BMC Medical Imaging

RESEARCH

Open Access

Development and internal validation of prediction model for rebleeding within one year after endoscopic treatment of cirrhotic varices: consideration from organ-based CT radiomics signature

Lulu Xu[1†], Jing Zhang[1†], Siyun Liu[2], Guoyun He[3] and Jian Shu[1*]

Abstract

Background Rebleeding after endoscopic treatment for esophagogastric varices (EGVs) in cirrhotic patients remains a significant clinical challenge, with high mortality rates and limited predictive tools. Current methods, relying on clinical indicators, often lack precision and fail to provide personalized risk assessments. This study aims to develop and validate a novel, non-invasive prediction model based on CT radiomics to predict rebleeding risk within one year of treatment, integrating radiomic features from key organs and clinical data.

Methods 123 patients were enrolled and divided into rebleeding ($n=44$) and non-bleeding group ($n=79$) within 1 year after endoscopic treatment of EGVs. The liver, spleen, and the lower part of the esophagus were segmented and the extracted radiomics features were selected to construct liver/spleen/esophagus radiomics signatures based on logistic regression. Clinic-radiomics combined models and multi-organ combined radiomics models were constructed based on independent model scores using logistic regression. The model performance was evaluated by ROC analysis, calibration and decision curves. The continuous net reclassification improvement (NRI) and integrated discrimination improvement (IDI) indices were analyzed.

Results The clinical-liver combined model had the highest AUC of 0.931 (95% CI: 0.887–0.974), which was followed by the liver-based model with AUC of 0.891 (95% CI: 0.835–0.74). The decision curves also showed that the clinical-liver combined model afforded a greater net benefit compared to other models within the threshold probability of 0.45 to 0.80. Significant improvements in discrimination (IDI, $P<0.05$) and reclassification (NRI, $P<0.05$) were obtained for clinical-liver combined model compared with the independent ones.

Conclusion The independent and combined liver-based CT radiomics models performed well in predicting rebleeding within 1 year after endoscopic treatment of EGVs.

†Lulu Xu and Jing Zhang contributed equally to this work.

*Correspondence:
Jian Shu
shujiannc@163.com

Full list of author information is available at the end of the article

Keywords Esophagogastric varices, Liver cirrhosis, Endoscopy, Tomography, X-Ray computed, Radiomics

Introduction

Esophagogastric (EGVs) are significant clinical manifestations of cirrhosis progression, affecting approximately 50% of cirrhotic patients, with a cumulative 10-year incidence rate of around 44% [1]. Esophagogastric variceal bleeding (EGVB) poses a substantial mortality risk, ranging from 10 to 20%, due to its acute onset, severe clinical presentation, and substantial hemorrhage [2]. Currently, endoscopy remains the gold standard for both diagnosis and treatment of EGVs, including endoscopic variceal ligation, injection sclerotherapy, and variceal obturation [3, 4]. Despite these interventions, the persistence of portal hypertension contributes to a high rebleeding rate, with up to 60% of patients experiencing rebleeding within the first year post-treatment, and mortality reaching as high as 30% [5]. Therefore, early identification of patients at high risk for rebleeding is critical for timely and effective secondary prevention and personalized treatment strategies.

Previous research has highlighted the utility of various non-invasive tests, such as laboratory assessments, radiological imaging, and ultrasound examinations, in predicting post-treatment prognosis of varices [6, 7]. However, these modalities are limited in their ability to directly visualize EGVs. In contrast, computed tomography (CT) offers a comprehensive depiction of the portal venous system and portosystemic collateral vessels. Importantly, CT imaging can visualize varices embedded deep within the mucosa, which are often indistinguishable from gastric mucosal folds on endoscopy [8, 9]. Assessing portosystemic collaterals, feeding vessels, and variceal volume via CT may enhance the prediction of rebleeding risk after endoscopic treatment and provide critical insights that inform subsequent therapeutic decisions [10–12].

Radiomics is an emerging field in medical imaging that offers the potential to quantitatively analyze radiological data. Radiomic features mathematically describe regions of interest (ROI), providing valuable quantitative insights into the spatial heterogeneity of tissues, which traditional imaging modalities may not capture [13]. It has shown excellent performance in various aspects, including cancer diagnosis, prognosis prediction, treatment response evaluation, and disease classification [14–16]. The application of radiomics is not limited to cancer; it also shows potential in the diagnosis and prognosis evaluation of cardiovascular diseases, neurodegenerative diseases, and cranial malformations [17–19]. Additionally, radiomics plays an increasingly important role in texture analysis, image annotation, and machine learning in medical imaging [20–22]. However, to the best of our knowledge, few studies have evaluated the utility of CT radiomics in predicting rebleeding following endoscopic treatment of esophageal and gastric varices (EGVs). This study aims to develop and internally validate CT-based radiomic signatures by independently or simultaneously analyzing the liver, spleen, and lower esophagus, and to assess their prognostic value for patients undergoing endoscopic treatment for EGVs. The use of CT radiomics directly addresses this challenge by identifying subtle imaging biomarkers related to increased rebleeding risk, such as changes in liver and vascular structure. By leveraging these radiomic features, our model enhances the early identification of high-risk patients, allowing for more personalized secondary prevention strategies and improving overall patient outcomes.

Materials and methods

Patients

This retrospective study was performed according to the Helsinki Declaration and approved by the ethics committee at the Affiliated Hospital of Southwest Medical University (ID: KY2020202). Patient consent for the study was waived as it was retrospective and anonymous. Cirrhotic patients with EGVs admitted to our hospital from January 2015 to December 2019 who received endoscopic therapy for the first time were enrolled and followed up for 1 year by telephone calls and a review of the hospital's medical record system. According to the follow-up results, patients were divided into a bleeding group (n=44) within 1 year after endoscopic treatment and a non-bleeding group (n=79). Inclusion criteria were: (1) CT examination before endoscopic treatment, and the interval not exceeding 2 months; (2) complete medical records and 1-year follow-up results; (3) patients included were those who experienced EGVB and subsequently underwent endoscopic treatment. (4) patients with esophageal varices only, GOV1 or GOV2 types according to Sarin typing were included [23]. The specifics of Sarin classification are in the supplemental document.

Exclusion criteria included: (1) liver and spleen/esophageal tumors; (2) surgical history of liver and spleen/esophageal. All of the enrolled patients underwent contrast-enhanced CT scans and serum tests. CT and laboratory examinations were performed just before the endoscopic treatment.

Image acquisitions

All patients underwent abdominal contrast-enhanced CT with a 256-detector CT scanner (Brilliance iCT, Philips Healthcare Systems, The Netherlands) and a 64-detector CT scanner (LightSpeed VCT, GE Healthcare Systems,

USA). The following parameters were used: tube voltage,120 kVp; tube current, 400–600 mA; and slice thickness, 5.0 mm. All patients received an intravenous, nonionic contrast medium (iodine concentration, 300–370 mg/mL; volume, 0.5–2.0 mL/kg of body weight; contrast medium type, Iohexol Injection, GE Healthcare) at a rate of 3–5 mL/s. A volume of 20 mL saline was injected after the injection of the contrast medium. Upper gastrointestinal endoscopy (GIF-HQ290, Olympus Tokyo, Japan) was performed after the CT examination. The treatment methods were selected according to the EGVs characteristics and CT findings.

Image segmentation and feature extraction

All the patients' image data were anonymized before analysis. An experienced radiologist blinded as to the patients' characteristics delineated the ROI in portal venous-phase CT images (hepatic hilum and splenic hilum planes, the most obvious layer of varicose veins in the lower esophagus) by using MaZda 4.6.2.0. Image intensity was firstly normalized into the range (μ − 3 SD, μ+3 SD; μ, mean intensity; SD, standard deviation of intensity) to minimize the influence of contrast and brightness variations. Next, six common textural feature groups (histogram, absolute gradient, gray-level co-occurrence matrix, run length matrix, autoregressive model, and wavelet transform) were extracted from MaZda, and a flow chart of the study is illustrated in Fig. 1. A total of 300 textural features were extracted from each ROI [23].

Intra- and inter-observer reliability assessment

Intra- and inter-observer reliability analyses were conducted to assess the repeatability of ROI segmentation and the extracted textural features. Thirty samples were randomly chosen from the final enrolled data in a blinded manner and evaluated by two radiologists. To evaluate the intra-observer agreement, the first radiologist delineated the ROI within 2 weeks following the same procedure. To assess the inter-observer agreement, the ROI segmentation was simultaneously performed once by the second radiologist with no discussion with the first radiologist. The intraclass correlation coefficient (ICC) was used to evaluate the intra-observer and inter-observer agreement for the extracted features based on the segmented ROIs. The feature reliability was classified as poor (ICC<0.5), moderate (0.5≤ICC<0.75), good (0.75≤ICC<0.9), or excellent (ICC≥0.9) [24]. The features with simultaneous intra- and inter-observer ICC>0.75 were used for further analysis.

Feature selection and model construction

There were eight representative models shown in the current study. The clinical model was constructed based on the clinical and CT radiographic characteristics, and the model risk score was derived to be further combined with the different radiomics models. In brief, the independent radiomics Radscore for each organ-based radiomics model (liver, spleen, and lower esophagus) was first derived. $Model^{Clinical+liver}$, $Model^{Clinical+spleen}$, and $Model^{Clinical\ +lower\ esophagus}$ were, respectively, a combination of the clinical risk score and the liver-, spleen-, and lower-esophagus-based radiomics Radscores. $Model\text{-}^{Liver\ +spleen}$ was constructed by combining the liver-based

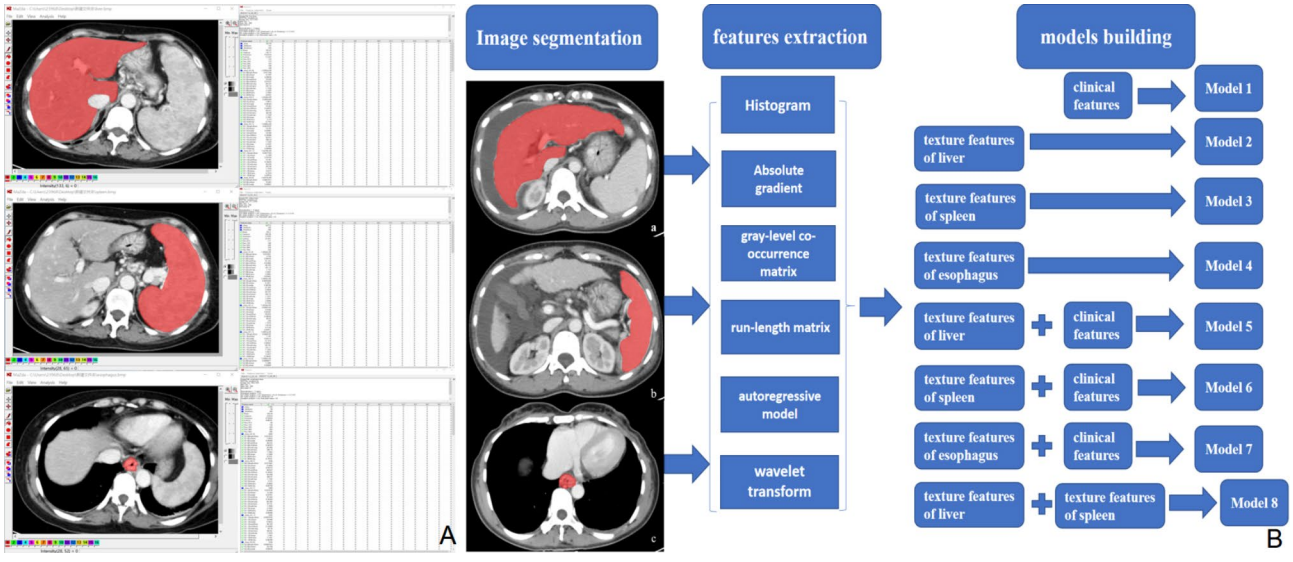

Fig. 1 Image segmentation and extracting data through MaZda software (**A**) and workflow of the key steps in the study (**B**). Based on the ROI segmentation for the liver, spleen, and lower esophagus in the CT images, about 300 textural features were extracted per organ. After feature selection, several independent and combined models were established based on the selected clinical and textural features

and spleen-based radiomics Radscores. Radscore is a numerical score that combines multiple radiomics features to create a single predictive index, which simplifies the model and enhances its interpretability [25, 26].

For the clinical model, the candidate features among the clinical factors and CT radiographic features were selected by using univariate and backward stepwise multiple logistic regression analysis according to the minimum Akaike information criterion. Then, the model score was calculated by the logistic regression method based on the retained features. In order to derive the three organ-based radiomics signatures or Radscores (liver, spleen, and lower esophagus), the same radiomics feature preprocessing, feature selection, and model construction procedure was sequentially performed, which was summarized in the supplementary material. All of the combined models were constructed from the model score or the Radscore of each independent model by directly using the logistic regression method.

Model evaluation and validation

The discrimination of the models was evaluated by the concordance (C)-statistic, which is equal to the area under the ROC curve when assessing two-class differentiation problems [27]. Meanwhile, sensitivity, specificity, and accuracy could also be derived to evaluate the model performance at the cut-off value determined as the Youden index reached the maximum. Delong's test was applied to examine the statistical difference in AUC values between paired models [28]. The model calibration, the agreement between the actual and predicted probability, was evaluated by calibration analysis [29]. The continuous net reclassification improvement (NRI) and integrated discrimination improvement (IDI) indices were analyzed to assess the added value of each independent model compared with the combined models [30]. The optimism-corrected estimation of AUC performance was also derived during 1000-times bootstrapping [31]. In addition, the clinical benefit brought by each model was also evaluated by decision curve analysis (DCA) [32].

Statistical analysis

The derived model risk score and the Radscores of the radiomics models were continuous variables. The remainder of the continuous variables among the clinical or CT manifestation predictors were categorized by using the cut-off value determined at the maximum Youden index in single-variable ROC analysis. All of the statistical analysis was performed using IBM SPSS statistics (version 25.0) and R software (version 3.5.3; http://www.r-project.org). The following R packages were mainly applied: "icc" – ICC calculation by setting a model of "two-way" and type of "agreement", "mRMRe" package – mRMR analysis, "glmnet" package – logistic regression including LASSO regression; "pROC" package – ROC analysis; "PredictABEL" package for continuous NRI and IDI indices calculation; and "rmda" package – DCA analysis.

Results

Patient characteristics

A total of 123 patients were recruited, and the baseline features of all patients are shown in Table 1. The study sample was divided into a rebleeding group consisting of 44 patients and a non-bleeding group consisting of 79 patients after endoscopic treatment. The rate of rebleeding was 35.77%.

Feature selection and model construction

For clinical model construction, there were seven features retained, and the logistic regression clinical model which derived the risk score $\text{Score}^{\text{Clinical}}$ summarized in Tables 2 and 3.

For each organ-based radiomics model, by using the same feature selection procedure, there were respectively four, one, and two features retained for the liver, spleen, and lower esophagus. The feature selection procedure for independent organ-based radiomics models was described in supplementary information. The logistic regression coefficients and the odds ratios for each selected feature in each independent model are summarized in Table 2.

The derived radiomics Radscores for the independent liver-, spleen-, and lower-esophagus-based logistic regression models and the combined model scores based on their combination with the clinical model or with each other are summarized in Table 3. The other combinations of different models are summarized in the supplementary information (Table S1).

The boxplot of each derived model score distributed in the non-rebleeding and rebleeding groups are shown in Fig. 2, all of which presented statistically significant differences between groups ($P<0.0001$).

Model performance evaluation

The ROC analysis results for each independent model or combined model are summarized in Table 4 and illustrated in Fig. 3(a). The AUC of the clinical model was 0.818 (95% CI: 0.740–0.895), and the accuracy was 77.2%. Among the independent radiomics models, the liver radiomics model had a better AUC of 0.891 (95% CI: 0.835–0.947) and an accuracy of 83.7%. Among the combined radiomics models, the clinical-liver model gave the highest AUC and accuracy of 0.931 (95% CI: 0.887–0.974) and 85.4%, respectively. Considering model overestimation during radiomics model construction, 1000-times bootstrapping was used for AUC optimism correction of the model. The overall performances of the

Table 1 Baseline clinical characteristics of enrolled patients

	Rebleeding within 1 year	Non rebleeding within 1 year	*P*
General Characteristics			
Male	32(72.727%)	56(70.886%)	0.256
Female	12(27.272%)	23(29.113%)	
Age (years)	50.47 ± 8.66	52.06 ± 11.37	0.814
Clinical Presentation			
Ascites	26(59.090%)	29(36.708%)	0.017*
Hepatic encephalopathy	1(2.273%)	0(0%)	0.178
Laboratory Parameters			
ALT(U/L)	28.750(20.500,39.600)	25.700(16.500,42.600)	0.438
AST(U/L)	38.300(31.025,63.340)	36.500(24.930,59.500)	0.246
TBIL(umol/L)	20.850(16.275,39.300)	22.700(14.500,33.200)	0.734
ALB(g/L)	31.700(28.500,35.3500)	32.500(29.500,37.500)	0.205
GGT	49.600(25.025,129.900)	44.100(27.700,99.500)	0.700
ALP	90.350(64.250,165.550)	82.800(65.400,124.800)	0.433
PT	16.900(14.950,18.300)	15.800(14.500,18.700)	0.179
INR	1.370(1.243,1.538)	1.280(1.180,1.570)	0.135
PLT($\times 10^9$)	67.500(42.000,90.250)	69.000(54.000,100.000)	0.283
RBC($\times 10^{12}$)	2.643 ± 0.643	2.924 ± 0.790	0.046*
NEU($\times 10^9$)	3.380(1.780,5.790)	3.070(1.900,4.780)	0.650
LYM($\times 10^9$)	0.730(0.540,1.365)	0.720(0.480,1.050)	0.200
WBC($\times 10^9$)	4.955(2.775,7.563)	4.300(3.120,6.270)	0.521
CT radiographic characteristics			
Portal vein diameter	1.641 ± 0 0.378	1.576 ± 0.332	0.331
Splenic vein diameter	1.630(1.475,1.833)	1.510(1.400,1.770)	0.931
Anterior and posterior diameter of spleen	13.955(11.965,14.918)	14.2000(12.390,15.870)	0.283
Left and right diameter of spleen	5.109 ± 1.026	5.214 ± 0.947	0.571
Upper and lower diameter of spleen	14.345(12.025,17.375)	15.000(13.400,17.600)	0.646
Portal vein or/and superior mesenteric vein thrombosis	7(15.909%)	17(21.518%)	0.438
Gastrorenal shunt	2(4.545%)	10(12.658%)	0.256

NotesALB albumin, *ALP* alkaline phosphatase, *ALT* alanine aminotransferase, *AST* aspartate aminotransferase, *GGT* γ-glutamyl transpeptidase, *INR* international normalized ratio, *LYM* lymphocyte count, *PLT* platelet count, *PT* prothrombin time, *RBC* red blood cell count, *TBIL* total bilirubin, *WBC* white blood cell count. Continuous variables are presented as the mean ± SD for a normal distribution or median (interquartile range) for a non-normal distribution. Categorical variables are presented as the frequency (%). *$P<0.05$, statistically significant level

radiomics models among the 1000-times bootstraps are summarized in Table 5. The respective optimism-corrected AUCs ($Model^{Liver}$ 0.849, $Model^{Spleen}$ 0.835, $Model^{Lower\ esophagus}$ 0.737) and average optimism ($Model^{Liver}$ 0.042, $Model^{Spleen}$ 0.002, $Model^{Lower\ esophagus}$ 0.03) represented the relatively good reliability of the models established from the selected features. At the same time, by combining the radiomics model with the clinical model, the model performance could be further enhanced compared with the independent clinical model or radiomics model (Delong's test with $P<0.05$). The combination of the liver-based radiomics model and the clinical model had an AUC of 0.931 (95% CI: 0.887–0.974), which was better than the spleen-based (AUC: 0.888, 95% CI: 0.819–0.956) or the esophagus-based (AUC: 0.867, 95% CI: 0.803–0.932) combined model.

As shown in Table S1, a significant improvement in discrimination (IDI, $P<0.05$) and reclassification (NRI, $P<0.05$) could be obtained by combining the clinical model with each organ-based radiomics model (liver or spleen) compared with the independent clinical or radiomics model. An obvious extent of model classification improvement was observed for the clinical-liver combined model when it was compared with the independent clinic model. The ROC curves in Fig. 3(a) also indicated the improved AUC performance for the combined model. The calibration curves in Fig. 3(b) showed that the liver-based models $Model^{Liver}$ and $Model^{Liver\ +clincal}$ had a better agreement between the predicted and observed probabilities, which were much closer to the 45-degree line with a slope of 1. Compared with other models, a higher net benefit for the clinical-liver combined model could be obtained in the threshold probability range 0.45–0.80 in the DCA curves as shown in Fig. 3(c).

However, no other combinations of the liver, spleen, esophagus, and clinical models significantly enhanced the AUC (Delong's test with $P>0.05$). The performance of all of the models and Delong's tests for the AUCs of

Table 2 The characteristics of each involved feature in each independent model during the multivariate logistic regression

Clinical characteristics	Coef.	Odds ratio (95% CI)	*P*
Diameter_PV	1.352	3.866(1.404–11.927)	0.012*
Spleen_UD	1.291	3.635(1.128–13.035)	0.036*
ALP	1.794	6.015(1.884–21.883)	0.004*
INR	0.806	2.238(0.804–6.708)	0.132
PLT	1.244	3.47(1.168–10.985)	0.028*
RBC	0.938	2.555(1.021–6.658)	0.048*
LYM	0.842	2.321(0.79–6.964)	0.126
Liver radiomics characteristics	**Coef.**	**Odds ratio (95% CI)**	***P***
X_MaxNorm	-2.165	0.115(0.048–0.229)	< 0.0001*
WavEnLH_s.6	-0.844	0.430(0.217–0.776)	0.009*
WavEnHH_s.7	-0.565	0.568(0.311–0.996)	0.054
X45dgr_GLevNonU	-0.665	0.514(0.268–0.938)	0.035*
Spleen radiomics characteristics	**Coef.**	**Odds ratio (95% CI)**	***P***
X_MaxNorm	-1.525	0.218(0.115–0.375)	< 0.0001*
Lower esophagus radiomics characteristics	**Coef.**	**Odds ratio (95% CI)**	***P***
Perc.99	-0.545	0.580(0.332–0.973)	0.045*
Variance	-0.851	0.427(0.208–0.808)	0.013*

**P* < 0.05, statistically significant level. *Coef* the logistic regression coefficient.*95%CI* 95% Confidence interval

the paired models are summarized in the Supplementary information (Table S2 and Table S3).

Discussion

Rebleeding represents a critical emergency, associated with substantial mortality and significant healthcare costs. In this study, the incidence of rebleeding following endoscopic treatment was 35.77%. The objective of this research is to develop non-invasive models based on CT radiomics features of various organs, enabling the identification of patient groups at high risk of rebleeding post-endoscopic intervention, and facilitating early intervention to improve prognosis. Among the organ-based CT radiomics models, the liver-based model demonstrated superior performance compared to the spleen- and esophagus-based models. Predictive accuracy was further enhanced by integrating the clinical model with the liver-based CT radiomics model. Some previous studies have shown that some laboratory data and imaging findings are associated with bleeding [33, 34] and rebleeding [35] of EGVs. To our knowledge, the higher the portal vein pressure the greater the risk of rebleeding [36]. In our study, factors that indirectly reflect portal vein pressure, such as portal vein diameter and upper and lower spleen diameters, were also found to be associated with rebleeding. Additionally, red blood cell (RBC) count and lymphocyte (LYM) count were identified as significant clinical indicators through multivariate logistic regression analysis and were incorporated into the predictive model. This may be attributed to the relationship between infection, anemia, and rebleeding risk [37, 38]. Furthermore, rebleeding was correlated with elevated alkaline phosphatase (ALP) levels, suggesting that patients with cholestasis may have a higher likelihood of rebleeding. The clinical model developed in our study demonstrated an area under the curve (AUC) of 0.818 and an accuracy of 77.2%. Some studies have proved that a CT radiomics model can noninvasively detect portal hypertension and predict the first bleeding [39–41]. Unlike previous models that focused on a single organ, our model integrates multiple organs, enhancing predictive accuracy. Portal hypertension is the primary cause of varices, indicating that CT radiomics offers a viable method for predicting rebleeding within one year following endoscopic treatment of EGVs. In this study, three independent organ-based radiomics models were constructed based on features extracted from CT images of the liver, spleen, and lower esophagus. Compared to the clinical model, the liver- and spleen-based radiomics models demonstrated superior diagnostic performance. In chronic liver disease, portal hypertension and EGVs result from increased resistance to portal blood flow due to significant structural changes in the liver vasculature,

Table 3 The scores of eight models

Model	Score
Clinical	$Score^{Clinical}$= -3.649 + 1.352×DiameterPV + 1.291×spleen_UD + 1.794×ALP + 0.805×INR + 1.244×PLT + 0.938×RBC + 0.842×LYM
Liver	$Radscore^{Liver} = -1.141 - 2.165 \times$ X_MaxNorm $- 0.844 \times$ WavEnLH_s.6 $- 0.565 \times$ WavEnHH_s.7 $- 0.665 \times$ X45dgr_GLevNonU
Spleen	$Radscore^{Spleen} = -0.852 - 1.525 \times$ X_MaxNorm
Lower esophagus	$Radscore^{Lower\ esophagus} = -0.820 - 0.545 \times$ Perc.99 $- 0.851 \times$ Variance
Clinical + liver	$Radscore^{Clinical+liver} = 0.465 + 0.868 \times Radscore^{Liver} + 0.77 \times Score^{Clinical}$
Clinical + spleen	$Radscore^{Clinical+spleen} = 0.35 + 0.789 \times Radscore^{Spleen} + 0.744 \times Score^{Clinical}$
Clinical + lower esophagus	$Radscore^{Clinical+lower\ esophagus} = 0.394 + 0.728 \times Radscore^{Lower\ esophagus} + 0.864 \times Score^{Clinical}$
Liver + spleen	$Radscore^{Liver+spleen} = 0.041 + 0.917 \times Radscore^{liver} + 0.132 \times Score^{Spleen}$

Notes Clinic independent clinical model, *Liver* independent liver radiomics model, *Spleen* independent spleen radiomics model, *Esophagus* independent esophagus radiomics model, *Clinic + Liver* combination of clinical and liver radiomics models, *Clinic + Spleen* combination of clinical and spleen radiomics models, *Clinic + Esophagus* combination of clinical and esophagus radiomics models, *Liver + Spleen* combination of liver and spleen radiomics model

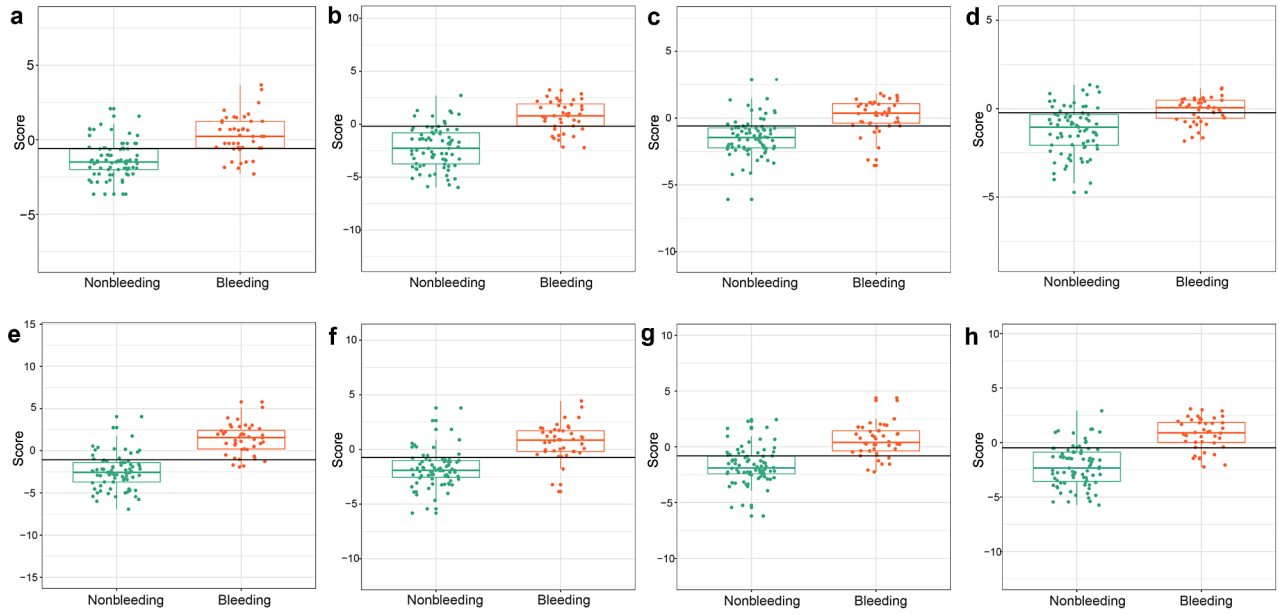

Fig. 2 The boxplot of each derived model score **(a–h)** distributed in the non-rebleeding and rebleeding groups. *Notes*: **(a)** based on clinical and CT radiographic characteristics; **(b)** liver-based radiomics model; **(c)** spleen-based radiomics model; **(d)** lower esophagus-based radiomics model; **(e)** combination of clinical with liver-based radiomics model; **(f)** combination of clinical with spleen-based radiomics model; **(g)** combination of clinical with lower-esophagus-based radiomics model; and **(h)** combination of liver-based radiomics with spleen-based radiomics model

including fibrosis, nodule formation, angiogenesis, and sinusoidal remodeling [42]. These pathophysiological alterations in the liver directly contribute to the development of EGVs, and the texture features of the liver can effectively capture changes in the liver's microenvironment [43]. In this study, the texture feature X_MaxNorm extracted from the liver and spleen, and Perc.99 and Variance extracted from the lower oesophagus could indicate the degree of change in brightness and pixel intensity values in CT imaging. These features may indicate that the degree of enhancement of the portal venous phase in the liver and spleen, as well as the brightness of the vessels in the lower oesophagus, are associated with rebleeding after endoscopic treatment. In addition, the texture roughness and complexity reflected by features WavEnLH_s.6, WavEnHH_s.7, and X45dgr_GLevNonU extracted from the liver may indicate the degree of structural remodelling within the liver.The irreversible microstructural changes within the liver are better represented by CT radiomics, making the liver-based model the most effective for predicting rebleeding. Of the three organ-based models, the lower esophagus model performed the least effectively, which may be due to the esophagus being in motion during CT scans, with the lower esophagus alternating between systolic and diastolic states. Additionally, our study utilized 2D images, which may not fully capture the varices in three dimensions. Future studies should consider incorporating 3D imaging to improve the comprehensiveness of these assessments.

Currently, the main scoring algorithms used clinically to predict rebleeding of esophagogastric varices include Glasgow Blatchford Score, pre-endoscopic Rockall Score, and AIMS65 Score, with an AUC value of 0.6–0.74 [44, 45]. While these scoring systems offer the advantages of simplicity and reduced cost, our predictive model demonstrates superior performance. This suggests that, despite the higher complexity and potential increased resource requirements, our model's enhanced predictive capabilities may provide more accurate and reliable outcomes. Our study on the prediction of esophagogastric variceal rebleeding after endoscopic treatment based on enhanced CT and Linxiang Liu's model [46] for predicting esophageal variceal rebleeding based on ultrasound Liver stifness measurements performed well, with AUC values of 0.8 or higher. However, compared with ultrasound liver stifness measurements, enhanced CT of the upper abdomen can visualize the anatomy and hemodynamics of the liver and the portal venous system.

The radiomics-clinic combined models outperformed both the standalone clinical and radiomics models. Among the combined models, the clinical-liver model achieved the highest AUC of 0.931 (95% CI: 0.887–0.974). In our study, additional combinations of liver, spleen, esophagus, and clinical models did not result in a significant increase in AUC. Although the extraction of imaging features and the construction of combination models were complex, these approaches did not demonstrate superior potential for clinical application. This highlights the fact that liver CT texture features provide

Table 4 Model performance for predicting rebleeding from the ROC analysis

Model	Clinical	Liver	Spleen	Lower esophagus	Clinical+liver	Clinical+spleen	Clinical +lower esophagus	Liver +spleen
AUC (95%CI)	0.818(0.740-0.895)	0.891(0.835-0.947)	0.838(0.758-0.917)	0.767(0.684-0.851)	0.931(0.887-0.974)	0.888(0.819-0.956)	0.867(0.803-0.932)	0.891(0.835-0.947)
Threshold	-0.584	-0.197	-0.585	-0.233	-1.069	-0.731	-0.808	-0.48
Specificity (95%CI)	0.759(0.648-0.845)	0.873(0.782-0.930)	0.810(0.710-0.881)	0.797(0.696-0.871)	0.823(0.724-0.891)	0.848(0.753-0.911)	0.759(0.655-0.840)	0.835(0.738-0.901)
Sensitivity (95%CI)	0.795 (0.655-0.888)	0.773(0.630-0.872)	0.841(0.706-0.921)	0.659(0.511-0.781)	0.909(0.788-0.964)	0.932(0.818-0.976)	0.864(0.733-0.936)	0.818(0.680-0.905)
Accuracy (95%CI)	0.772 (0.691-0.838)	0.837(0.762-0.892)	0.821(0.744-0.879)	0.748(0.665-0.816)	0.854(0.781-0.905)	0.878(0.808-0.925)	0.797(0.717-0.858)	0.829(0.753-0.886)
NPV (95%CI)	0.87(0.770-0.930)	0.873(0.782-0.930)	0.901(0.810-0.951)	0.808(0.707-0.880)	0.942(0.860-0.977)	0.957(0881-0.985)	0.909(0.815-0.958)	0.892(0.801-0.944)
PPV (95%CI)	0.648(0.515-0.762)	0.773(0.630-0.872)	0.712(0.577-0.817)	0.644(0.498-0.777)	0.741(0.611-0.839)	0.774(0.645-0.865)	0.667(0.537-0.775)	0.735(0.597-0.838)

Clinic independent clinical model, *Liver* independent liver radiomics model, *Spleen* independent spleen radiomics model, *Esophagus* independent esophagus radiomics model, *Clinic + Liver* combination of clinical and liver radiomics models, *Clinic + Spleen* combination of clinical and spleen radiomics models, *Clinic + Esophagus* combination of clinical and esophagus radiomics models, *Liver + Spleen* combination of liver and spleen radiomics mode

an accurate and objective reflection of changes in the liver microenvironment. Consequently, both the liver radiomics model and the clinical-liver combined model are grounded in sound clinical reasoning for predicting the likelihood of rebleeding. Moreover, the non-invasive CT radiomics model offers a simple and cost-effective approach for rebleeding prediction, which may facilitate broader patient acceptance. Clinical data and features taken from medical imaging are combined to create a clinical+radiomics model. This model is highly interpretable and can be advantageous in offering a natural understanding of diseases because the chosen features are directly correlated with the pathophysiological processes of diseases. While deep learning models are capable of processing a greater variety of input formats, their "black box" design prevents logical justifications for the features that are chosen [40, 47]. Furthermore, the clinical+radiomics model is easy to develop and utilize in clinical settings, and it does not require any specialized hardware or software like deep learning models do.

There are some limitations in this study. First, the limited sample size of the included cases presents a challenge, as it often leads to data imbalance. This issue arises when the model training process involves one category with significantly more samples than others, potentially causing the model to perform well in the majority class while underperforming in the minority classes. As a result, the overall predictive accuracy and utility of the model may be compromised. In addition to increasing the sample size, some studies have addressed this problem by applying various data balancing techniques, which enhance dataset balance and improve the model's predictive performance [48, 49]. Meanwhile, model overfitting can diminish the generalizability of results and lead to suboptimal performance when applied to other datasets. We are actively working to collect more data and implement data balancing methods to enhance the model's generalizability. Second, the study lacks multi-center controlled trials and external validation. To address this limitation, we implemented image standardization, evaluated feature reliability using intraclass correlation coefficient (ICC), and performed internal validation through 1,000 bootstrapped samples to enhance the robustness of the model. Third, the use of the largest cross-sectional area of the organ in this study may have resulted in the loss of critical information. Fourth, while our current study extracted 2D images of the lower esophagus, which may not fully capture the three-dimensional characteristics of varicose veins, we intend to incorporate continuous 3D imaging in our subsequent studies to enhance the depth of our analysis. Fifthly, the retrospective nature of this study may introduce selection bias. To mitigate this limitation, we plan to undertake prospective studies in the future.

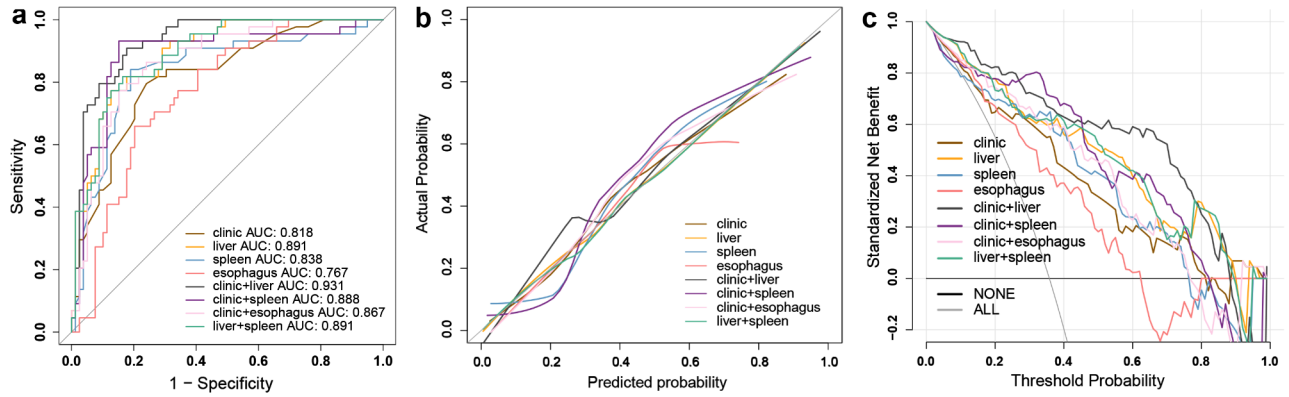

Fig. 3 Illustration of model performance. **(a)** The ROC curves of eight models. **(b)** The calibration curves of eight Models, which describe the agreement between the model predicted probability and actual event happening probability. **(c)** The decision curves of eight models. *Notes*: The black horizontal line assumes no patients with rebleeding (NONE) and the grey line assumes all patients with rebleeding (ALL). The colored lines of each model illustrate the net benefit brought to each patient by choosing different threshold probability. The closer the decision curves are to the black and gray curves, the lower the clinical decision net benefit of the model. When comparing the net benefit among different models within specific threshold probability range, the higher the model curve, the greater the clinical usefulness

Table 5 1000-times bootstrap estimate of the area under the ROC curve and the model optimism estimation

Index	Model	Apparent AUC[a]	AUC Bootstrap-Train[b] (mean, 95% CI)	AUC Bootstrap-Test[c] (mean, 95% CI)	Average optimism[d]	Optimism-corrected AUC[e]
1	Liver	0.891	0.898(0.896-0.9)	0.856(0.853–0.858)	0.042	0.849
2	Spleen	0.837	0.839(0.836–0.841)	0.837(0.833–0.840)	0.002	0.835
3	Esophagus	0.767	0.773(0.770–0.775)	0.742(0.738–0.745)	0.03	0.737

Notes a. The AUC of the predicting model developed in the original whole dataset

b. The averaged model performance in the resampled training set after 1000-times bootstrapping

c. The averaged model performance in the "out-of-bag" test set after 1000-times bootstrapping

d. The averaged optimism of the model as the difference between the bootstrap training set AUC and the test AUC

e. The corrected AUC was found by subtracting the average optimism from the apparent AUC

In future work, we will focus on conducting multicenter studies to externally validate the model across diverse patient populations, enhancing its generalizability. We will also explore the use of 3D imaging techniques to capture more comprehensive variceal features and investigate the application of deep learning approaches for automated ROI segmentation and feature extraction. Additionally, we aim to explore image-based deep learning methods that do not require manual ROI segmentation. Prospective clinical studies will further refine and implement the model in real-time settings, ensuring its practicality and robustness in clinical applications.

Conclusion

In conclusion, the clinical-liver combined model could have the potential to evaluate the prognosis of endoscopically treated patients, suggesting that radiomics-enhanced CT assessments could be routinely integrated into patient management. By enabling personalized risk stratification, this model could guide clinicians in making more informed decisions about the intensity of follow-up and the need for secondary prophylaxis, ultimately improving patient outcomes and reducing mortality. To our knowledge, this study may have derived the first CT-based radiomics models to consider multiple organs for predicting rebleeding after endoscopic treatment of cirrhotic varices. An unexpected finding was the comparatively lower performance of the esophageal-based radiomics model, likely due to the anatomical challenges of capturing dynamic structures during CT scans. This highlights the potential for future studies to incorporate advanced imaging techniques such as 3D CT or motion correction algorithms to improve diagnostic accuracy. Furthermore, the broader application of radiomics in cirrhotic complications, such as portal hypertension or hepatocellular carcinoma, could stimulate further research and innovation in predictive imaging.

Abbreviations

EGVs	Esophagogastric varices
EGVB	Esophagogastric variceal bleeding
ICC	Intraclass correlation coefficient
NRI	Net reclassification improvement
IDI	Integrated discrimination improvement
DCA	Decision curve analysis
RBC	Red blood cell count
LYM	Lymphocyte count
ALP	Alkaline phosphatase

Supplementary Information

The online version contains supplementary material available at https://doi.org/10.1186/s12880-024-01461-8.

Supplementary Material 1

Acknowledgements
The authors acknowledge the other members for their contributions to the research, including linlin guo, liming wang, xiaofeng wang, chunmei yang, mengpin huang.

Author contributions
LX, JZ and SL analyzed data. LX drafted the manuscript text. GH, LX and JS substantively revised the manuscript text. LX, JZ, SL and GH acquired CT data. All authors read and approved the final manuscript.

Funding
This research did not receive any specific grant from funding agencies in the public, commercial, or not-for-profit sectors.

Data availability
The original contributions presented in the study are included in the article/Supplementary Material. Further inquiries can be directed to the corresponding author.

Declarations

Ethical statement
This retrospective study was performed according to the Helsinki declaration and approved by the ethics committee at the Affiliated Hospital of Southwest Medical University (ID: KY2020202).
The patient's informed consent for the study was waived as it was retrospective and anonymous.

Consent for publication
Not Applicable.

Competing interests
Author Siyun Liu was employed by GE Healthcare, Beijing, China. The remaining authors declare that the research was conducted in the absence of any commercial or financial relationships that could be construed as a potential conflictof interest.

Author details
[1]Department of Radiology, The Affiliated Hospital of Southwest Medical University, NO. 25, Taiping Road, Jiangyang District, Luzhou City, Sichuan, China
[2]Pharmaceutical Diagnostics, GE Healthcare, Beijing, China
[3]The Affiliated Traditional Chinese Medicine Hospital of Southwest Medical University, Luzhou, China

Received: 20 April 2024 / Accepted: 9 October 2024
Published online: 29 October 2024

References

1. D'Amico G, Pasta L, Morabito A, D'Amico M, Caltagirone M, Malizia G, et al. Competing risks and prognostic stages of cirrhosis: a 25-year inception cohort study of 494 patients. Aliment Pharmacol Ther. 2014;39:1180–93.
2. Amitrano L, Guardascione MA, Manguso F, Bennato R, Bove A, DeNucci C, Lombardi G, Martino R, Menchise A, Orsini L, Picascia S, Riccio E. The effectiveness of current acute variceal bleed treatments in unselected cirrhotic patients: refining short-term prognosis and risk factors. Am J Gastroenterol. 2012;107(12):1872–8.
3. Seo YS. Prevention and management of gastroesophageal varices. Clin Mol Hepatol. 2018;24:20–42.
4. de Franchis R, Baveno VI. Expanding consensus in portal hypertension: report of the Baveno VI Consensus Workshop: stratifying risk and individualizing care for portal hypertension. J Hepatol. 2015;63:743–52.
5. Jono F, Iida H, Fujita K, Kaai M, Kanoshima K, Ohkuma K, et al. Comparison of computed tomography findings with clinical risks factors for endoscopic therapy in upper gastrointestinal bleeding cases. J Clin Biochem Nutr. 2019;65:138–45.
6. Jiménez Rosales R, Martínez-Cara JG, Vadillo-Calles F, Ortega-Suazo EJ, Abellán-Alfocea P, Redondo-Cerezo E. Analysis of rebleeding in cases of an upper gastrointestinal bleed in a single center series. Rev Esp Enferm Dig. 2019;111:189–92.
7. TGarcia-Pagán JC, Patch D. Trials and tribulations: the Prevention of Variceal rebleeding. Gastroenterology. 2015;149(3):528–31.
8. Li Q., Wang R, Guo X, et al. Contrast-enhanced CT may be a Diagnostic Alternative for Gastroesophageal Varices in cirrhosis with and without previous endoscopic variceal therapy. Gastroenterol Res Pract. 2019;2019:6704673.
9. Gupta A, Gamangatti S, Sharma S, Gopi S, Hemachandran N, Saraya A. Aberrant collaterals in Cirrhosis and challenges in its management. J Clin Exp Hepatol 2023 May-Jun;13(3):542–6.
10. Rice JP, Lubner M, Taylor A, Spier BJ, Said A, Lucey MR, et al. CT portography with gastric variceal volume measurements in the evaluation of endoscopic therapeutic efficacy of tissue adhesive injection into gastric varices: a pilot study. Dig Dis Sci. 2011;56:2466–72.
11. Kodama H, Aikata H, Takaki S, Azakami T, Katamura Y, Kawaoka T, et al. Evaluation of portosystemic collaterals by MDCT-MPR imaging for management of hemorrhagic esophageal varices. Eur J Radiol. 2010;76:239–45.
12. Lee HA, Goh HG, Kim TH, Lee YS, Suh SJ, Jung YK, Chun HJ, Byun KS, Um SH, Kim CD, et al. Evaluation of treatment response after endoscopic Variceal Obturation with Abdominal computed Tomography. Gut Liver. 2020;14:117–24.
13. Davnall F, Yip CS, Ljungqvist G, Selmi M, Ng F, Sanghera B, et al. Assessment of tumor heterogeneity: an emerging imaging tool for clinical practice? Insights Imaging. 2012;3:573–89.
14. Zhang Y, Duan J, Sa Y, Guo Y. Multi-atlas based adaptive active Contour Model with Application to organs at Risk Segmentation in Brain MR images. IRBM. 2020;42(6):351–8.
15. Bakkouri I, Afdel K, DermoNet:. A computer-aided diagnosis system for Dermoscopic Disease Recognition. In: El Moataz A, Mammass D, Mansouri A, Nouboud F, editors. Image and Signal Processing. ICISP 2020. Lecture Notes in Computer Science. Volume 12119. Cham: Springer; 2020. pp. 170–7.
16. Liu J, Chen Q, Zhang Y, Wang Z, Deng X, Wang J. Multi-level feature fusion network combining attention mechanisms for polyp segmentation. Comput Biol Med. 2024;169:107931.
17. Mohtasebi M, Bayat M, Ghadimi S, Abrishami Moghaddam H, Wallois F. Modeling of neonatal Skull Development using computed tomography images. IRBM. 2020;42(2):101–8.
18. Veluppal A, Sadhukhan D, Gopinath V, Swaminathan R. Detection of mild cognitive impairment using Kernel Density Estimation based texture analysis of the Corpus Callosum in Brain MR images. IRBM. 2021;43(4):301–8.
19. Xu X, Wu R, Zhang W, Ding G, Liu L, Chi M, Xie J, Huang L. Multi-feature Fusion Method for identifying carotid artery vulnerable plaque. IRBM. 2021;43(5):351–8.
20. He S, Wu J, Lian C, Gach HM, Mutic S, Bosch W, Michalski J, Li H. An adaptive low-rank modeling-based active learning method for Medical Image Annotation. IRBM. 2021;42(5):334–44.
21. Veluppal A, Sadhukhan D, Gopinath V, Swaminathan R. Detection of mild cognitive impairment using Kernel Density Estimation based texture analysis of the Corpus Callosum in Brain MR images. IRBM. 2022;43(5):340–8.
22. Yadav N, Dass R, Virmani J. Deep learning-based CAD system design for thyroid tumor characterization using ultrasound images. Multimed Tools Appl. 2024;83:43071–113.
23. Bazarbashi A, Ryou M. Gastric variceal bleeding. Curr Opin Gastroenterol. 2019;35(6):524–34.
24. Szczypiński PM, Strzelecki M, Materka A, Klepaczko A. MaZda–a software package for image texture analysis. Comput Methods Programs Biomed. 2009;94:66–76.
25. Koo TK, Li MY. A Guideline of selecting and reporting Intraclass correlation coefficients for Reliability Research. J Chiropr Med. 2016;15:155–63.
26. Shao J, Jiang Z, Jiang H, et al. Machine learning Radiomics liver function model for Prognostic Prediction after Radical Resection of Advanced Gastric Cancer: a retrospective study. Ann Surg Oncol. 2024;31:1749–59.

27. Gerds TA, Cai T, Schumacher M. The performance of risk prediction models. Biometrical J Biometrische Z. 2010;50:457–79.
28. Sun C, Liu X, Sun J, et al. A CT-based radiomics nomogram for predicting histopathologic growth patterns of colorectal liver metastases. J Cancer Res Clin Oncol. 2023;149:9543–55.
29. Harrell FE Jr, Lee KL, Mark DB. Multivariable prognostic models: issues in developing models, evaluating assumptions and adequacy, and measuring and reducing errors. Stat Med. 1996;15:361–87.
30. Pepe MS, Kerr KF, Longton G, Wang Z. Testing for improvement in prediction model performance. Stat Med. 2013;32:1467–82.
31. Moons KG, Altman DG, Reitsma JB, Ioannidis JP, Macaskill P, Steyerberg EW, et al. Transparent reporting of a multivariable prediction model for individual prognosis or diagnosis (TRIPOD): explanation and elaboration. Ann Intern Med. 2015;162:W1–73.
32. Huang YQ, Liang CH, He L, Tian J, Liang CS, Chen X, et al. Development and validation of a Radiomics Nomogram for Preoperative Prediction of Lymph Node Metastasis in Colorectal Cancer. J Clin Oncol. 2016;34:2157–64.
33. Heo JY, Kim BK, Park JY, Kim DY, Ahn SH, Tak WY, et al. Multicenter Retrospective Risk Assessment of Esophageal Variceal bleeding in patients with cirrhosis: an Acoustic Radiation Force Impulse Elastography-based prediction model. Gut Liver. 2019;13:206–14.
34. Calame P, Ronot M, Bouveresse S, Cervoni JP, Vilgrain V, Delabrousse É. Predictive value of CT for first esophageal variceal bleeding in patients with cirrhosis: value of para-umbilical vein patency. Eur J Radiol. 2017;87:45–52.
35. Jeong SW, Kim HS, Kim SG, Yoo JJ, Jang JY, Lee SH, et al. Useful endoscopic ultrasonography parameters and a predictive model for the recurrence of esophageal varices and bleeding after Variceal Ligation. Gut Liver. 2017;11:843–51.
36. Addley J, Tham TC, Cash WJ. Use of portal pressure studies in the management of variceal haemorrhage. World J Gastrointest Endosc. 2012;16(7):281–9.
37. Pohl J, Pollmann K, Sauer P, Ring A, Stremmel W, Schlenker T. Antibiotic prophylaxis after variceal hemorrhage reduces incidence of early rebleeding. Hepatogastroenterology. 2004;51:541–6.
38. Daba M, El-Halabi K, El-Din A, et al. Incidence and predictors of rebleeding after band ligation of oesophageal varices. Arab J Gastroenterol. 2014;15(3–4):135–41.
39. Yang JQ, Zeng R, Cao JM, Wu CQ, Chen TW, Li R et al. Predicting gastro-oesophageal variceal bleeding in hepatitis B-related cirrhosis by CT radiomics signature. Clin Radiol. 2019;74:976.e1-976.e9.
40. Wang J, Wang Z, Chen M, et al. An interpretable artificial intelligence system for detecting risk factors of gastroesophageal variceal bleeding. Npj Digit Med. 2022;5:183.
41. Gao Y, Yu Q, Li X, et al. An imaging-based machine learning model outperforms clinical risk scores for prognosis of cirrhotic variceal bleeding. Eur Radiol. 2023;33:8965–73.
42. Brunner F, Berzigotti A, Bosch J. Prevention and treatment of variceal haemorrhage in 2017. Liver Int. 2017;37(Suppl 1):104–15.
43. Brown RA, Frayne R. A comparison of texture quantification techniques based on the Fourier and S transforms. Med Phys. 2008;35:4998–5008.
44. Robertson M, Ng J, Abu Shawish W, Swaine A, Skardoon G, Huynh A, Deshpande S, Low ZY, Sievert W, Angus P. Risk stratification in acute variceal bleeding: comparison of the AIMS65 score to established upper gastrointestinal bleeding and liver disease severity risk stratification scoring systems in predicting mortality and rebleeding. Dig Endoscopy. 2020;32:761–8.
45. Budimir I, Gradišer M, Nikolić M, Baršić N, Ljubičić N, Kralj D, Budimir I jr. Glasgow Blatchford, pre-endoscopic rockall and AIMS65 scores show no difference in predicting rebleeding rate and mortality in variceal bleeding. Scand J Gastroenterol. 2016;51(11):1375–9.
46. Li Z, Chen Y, Li X, et al. A practical model for Predicting Esophageal Variceal rebleeding in patients with Hepatitis B-Associated cirrhosis. Dig Dis Sci. 2018;63(4):1042–9.
47. Malik S, Tenorio BG, Moond V, Dahiya DS, Vora R, Dbouk N. Systematic review of machine learning models in predicting the risk of bleed/grade of esophageal varices in patients with liver cirrhosis: a comprehensive methodological analysis. J Gastroenterol Hepatol. 2024.
48. Chandrasekar V, et al. Investigating the Use of Machine Learning models to understand the drugs permeability across Placenta. IEEE Access. 2023;11:52726–39.
49. Ansari MY, Chandrasekar V, Singh AV, Dakua SP. Re-Routing Drugs to Blood Brain Barrier: A Comprehensive Analysis of Machine Learning Approaches With Fingerprint Amalgamation and Data Balancing, in *IEEE Access*, vol. 11, pp. 9890–9906, 2023.

Publisher's note